Fish-eye Distortion Correction, Image Super Resolution and MEG Data Analysis

A Project Report

submitted by

GREEN ROSH K S

in partial fulfilment of requirements
for the award of the dual degree of

BACHELOR OF TECHNOLOGY AND MASTER OF TECHNOLOGY

DEPARTMENT OF ELECTRICAL ENGINEERING
INDIAN INSTITUTE OF TECHNOLOGY MADRAS

MAY 2017

THESIS CERTIFICATE

This is to certify that the thesis titled **Fish-eye Distortion Correction, Image Super Resolution and MEG Data Analysis**, submitted by **Green Rosh K S**, to the Indian Institute of Technology, Madras, for the award of the degree of **Master of Technology**, is a bona fide record of the research work done by him under our supervision. The contents of this thesis, in full or in parts, have not been submitted to any other Institute or University for the award of any degree or diploma.

Dr. A N Rajagopalan

Professor
Dept. of Electrical Engineering
IIT-Madras, 600 036

Place: Chennai

Date: 2nd May 2017

ACKNOWLEDGEMENTS

I take this opportunity to express my deepest gratitude to my project guide Dr. A.N. Rajagopalan for his valuable guidance and motivation throughout the project. I am very grateful to him for providing his valuable time to guide me during the project.

I would also like to thank Dr. Jyotirmoy and Vibhin Viswanathan of National Brain Research Centre, Gurgaon, for helping me with my project and guiding me through an alien subject. I am also indebted to Abhijith Punnapurath and Vijay Rengarajan, who advised me throughout the project and helped me when I got stuck. I also thank my colleagues, Subheesh, Mahesh, Nimisha, Kuldeep, Arun and Karthik who advised me with their wisdom throughout my stay in the lab.

Finally, I am extremely thankful for my parents, for believing in me, for my teachers, for the academic insight that they provided, and my friends, Sreyas, Akash, Pranoy and several others for their support.

ABSTRACT

KEYWORDS: Fish-eye camera ; 360^o panorama; Image super resolution; Rolling shutter effect; Global shutter cameras; Motion blur; Alternating Minimisation; Magnetoencephalography; Epilepsy; Coherence

From medical imaging to self-driving cars, the role of post processing in imaging systems is increasing at an exponential rate. In this thesis, we identify and solve three different problems from three different domains.

In applications such as self-driving cars, a full 360^o view of the world is often required to make quick decisions in real time. The limited Field-of-View (FOV) of conventional cameras make the imaging system bulky. Also, the processing required to stitch several images may not be feasible in real time. Wide-angle cameras such as fish-eye cameras offer a hardware solution to this problem. An imaging system consisting of two back-to-back fish eye cameras can capture the whole 360^o world. However these images are affected by barrel distortion due to their projection models. To make image processing efficient, it is required to convert these images to rectilinear domain before attempting to stitch the panorama. In this thesis, we use geometric projection models to rectify the distortion induced by fish eye cameras. We propose an algorithm that works with the knowledge of FOV alone, and camera calibration is not required.

For the second problem, we consider the domain of image super-resolution. The need for images with better resolution has been rising steady over the past few years with the abundance of consumer cameras available in the market. However, the maximum resolution that the camera hardware can support is limited by both space and cost constraints. Image super-resolution offers an image processing solution to this problem. Conventional super-resolution algorithms, however work for images captured in stationary environment and do not take into account the camera motion during exposure. We propose an alternating-minimisation based algorithm that super resolves low resolution images captured in the presence of camera motion, for CMOS cameras used in smart phones, where motion blur and rolling shutter effect degrades the quality of the

image.

For our third problem, we consider Magnetoencephalography (MEG) signals used in the imaging of the brain. MEG data can be used to analyse the brain waves during various states of activities. In particular, we analyse the MEG signals for a subject with drug resistant epilepsy. During an episode of epileptic discharge, it is observed that the connectivity among various regions of the brain increases. We use coherence as a measure of connectivity, and also explores if the increase in coherence between pairs of sensors can be used to detect epilogenetic regions in the brain

TABLE OF CONTENTS

LIST OF TABLES

LIST OF FIGURES

ABBREVIATIONS

FOV	Field of View
HR	High Resolution
LR	Low Resolution
SR	Super Resolution
MB	Motion Blur
RS	Rolling Shutter
GS	Global Shutter
AM	Alternating Minimization
MCBD	Multi-Channel Blind Deblurring
MEG	Magnetoencephalography
EEG	Electroencephalography
tSSS	temporal Signal Space Seperation
PSD	Power Spectral Density

NOTATION

$\mathbf{U}$	Latent HR image
$\mathbf{u}$	HR image vector
$\boldsymbol{\mathcal{H}}$	Warping Matrix
$\boldsymbol{D}$	Decimation Matrix
$\boldsymbol{v}$	LR image vector
$\boldsymbol{\mathcal{P}}$	Camera Motion Trajectory
α	Row exposure time
β	Inter-row delay time
$\boldsymbol{r_i}$	i^{th} row
$\boldsymbol{\theta_k}$	Trajectory coefficients for k^{th} image
$\boldsymbol{J}$	Jacobian
γ	Coherence
S	Power spectral density / cross spectral density

CHAPTER 1

Introduction

Image processing and its associated fields find applications in a wide spectrum of fields from meteorology to medicine. Conventional image processing algorithms aim at image enhancement, trying to eliminate various artefacts introduced by the imaging process. In conventional photography, image processing find use in applications such as image de-blurring, image warping and image super resolution. Also, inaccurate image capturing techniques result in distortions such as rolling shutter effect or barrel distortion in the image. Research in classical image processing aim to rectify these problems. There has also been an increase of image processing in domains such as medical imaging. Medical imaging aims both at artefact reduction, such as in MRI, as well in image analysis, such as MEG analysis. In this thesis, we consider the applications of image processing in image distortion correction, image super resolution, image de-blurring and panorama stitching. We also analyse medical imaging data originated from brain MEG, to observe coherent regions in the brain.

1.1 Distortion Correction in Fish-eye Images

With the advent of new technologies such as virtual reality and self-driving cars, the significance of 360^o images and videos are increasing exponentially. However, conventional camera provide a field of view (FOV) of merely 60^o and this hinders the process of acquiring a 360^o image. Hence there is a growing research on the development of cameras with a large FOV. In the literature, several methods have been proposed to increase the FOV of cameras [1].The first one consists of a moving camera set up, which captures images and then combines them, which may not be feasible in a real time setting. A second solution consists of combining conventional cameras and mirrors. These type of sensors are called catadioptric systems. However, these systems create a dead spot at the center of the image, which cannot be removed. Also, the presence of mirrors causes the system to be bulky. The last class of camera with a wide field of view belong to the class of dioptric systems. Fish-eye camera,which uses fish eye lens to generate really wide angle images belongs to this category. They can produce images with FOV of 180^o and upward, without introducing any dead or blind spots. Hence, a 360^o image can easily be obtained by a system of 2 fish eye lens aligned back to back and can be processed easily in real time.

Fish-eye cameras produce images with high FOV by foregoing the rectilinear mapping common in conventional cameras and seeking for mappings that map the entire frontal hemispherical scene on to a flat surface. Hence this produces a severe barrel distortion in the image. As a result, the image looks as if it has been stretched about a sphere which causes the straight lines in the real images to bulge outwards and curved. Due to this distortion, the stitching of fish-eye images is a non-trivial task, and requires certain simplifying assumptions. In this thesis, we discuss an algorithm to rectify the distortion causes about by the fish eye camera, and also how to stitch two fish eye images together to obtain a 360^o view.

1.1.1 Related Works

There has been several research works on image distortion correction for wide angle and conventional cameras. [7] talks about a lens distortion model for general cameras. The fish eye camera is explored in detail in [2]. [5] and [6] explores the various calibration techiniques used in wide angle cameras. There has also been significant research in panoramic stitching of fish eye images such as [4] where, panorama is created using point correspondences in fish eye images. Application of 360^o are also popular such as [3], where object tracking in full-view panorama is explored.

1.1.2 Contributions

- Our algorithm rectifies the barrel distortion obsereved in fish eye images without the knowledge of intrinsic camera parameters. Even in the absence of camera calibration, our algorithm works excellent for full frame fish eye, with the knowledge of FOV, where the assumption of equidistant image is valid.
- We also propose an algorithm to combine two fish-eye images to produce a full 360^o panorama.

1.2 Super Resolution with Motion Artefacts

With the ever-growing demand for high resolution images and videos, image super-resolution becomes an important area of research, which offers a signal processing solution to otherwise, an inherently hardware oriented problem. In multi-image super resolution (SR), the goal is to recover a high-resolution image (HR) from multiple low-resolution (LR) images. The principle behind multi-image super resolution is that the inevitable camera motion between images introduces new information to each new image. The super resolution attempts to create HR images from this additional information available in each subsequent image. Super resolution models assume a latent HR image, onto which pose matrices are applied to obtain images in different poses. These images get down-sampled in the camera sensor array to produce the LR images. If the poses or the *in-between* matrices are known, then the problem becomes a straight forward estimation of the latent HR image. However, in most cases, the information on the pose is unknown, making the SR problem hard and ill-posed.

Classical image SR algorithms try to handle the *in-between* image motion. But they do not take into account the handshake which happens during image exposure, which results in a camera motion *during* the image capture. This further worsens the problem. In a standard CCD sensor, which is used in most digital cameras, the whole camera sensor space is exposed at once to the image. Hence any motion encountered by the camera affects the scene as a whole. These kinds of cameras are generally called global shutter cameras (GS). Any camera motion during the exposure time period, hence manifests as a motion blur (MB) artefact in the final image, which cannot be handled by traditional SR algorithms.

This problem is further aggravated in CMOS sensors, which are used in smartphone cameras. To save buffer space. these cameras use a rolling shutter, wherein only a few rows in the sensor array are exposed at any given time. For this reason, these cameras are also called rolling shutter cameras (RS). In these types of cameras, each row experiences a different camera motion as compared to other rows. Hence, we have to solve not just for a single camera pose or motion, but for multiple camera motions. These camera motions introduce an artefact which we call RS affect. The RS effect distorts images according to the camera motion. Hence an actual straight line in a scene may appear sheared or curved in the image depending on the camera motion. A motion blur may also be introduced depending on the camera motion during row exposure time. In this chapter, an algorithm which attempts to solve multi-image super resolution problem in the presence of RS and MB artefacts is discussed.

1.2.1 Related Works

Classical multi-image super resolution is an extensively researched topic. [8] provides an excellent overview of various super resolution techniques available. The early works on super resolution focusses mainly in the frequency domain, as pioneered by Tsai and Hung in their seminal paper [9]. However the frequency domain approaches are limited in the images they can handle and performed poorly on complex real world examples. Researchers have shifted their focus onto spatial domain approaches.

In addition to multi-image super resolution, hallucination based single image super-resolution techniques are on the rise. These methods, learn relations between LR and HR image patches, and use these priors on new problems [10]. [11] uses deep convolutional neural networks to solve the single image super resolution problem. However the learning based SR algorithms, tend to introduce image patches that might not be present in the actual image (hallucinations).

The above mentioned works assume a stationary camera and do not account for RS or MB effects. [12] uses introduces multi-channel blind deconvolution, which super resolves LR images affected by space invariant blur. [13] extends this problem to include space invariant blur. In [14], the authors try to solve super-resolution problem for RS affected (but no motion blur) LR images under the constraint that atleast one image in RS free. [15] removes this constraint, but adds an additional constraint of burst mode.

1.2.2 Contributions

- Our work, as opposed to previous works on multi-image SR, attempts to solve for LR images affected by both MB as well as SR

- Also, our model rectifies image artefacts on the knowledge of exposure time parameters, and no other assumptions are made.

1.3 Analysis of MEG Data

The human brain is a vast network of connected pathways that communicate through synchronized electric brain activity along neurons. Methods such as EEG and MEG can used to detect the electrical and magnetic activities in the brain. This data can further be analysed to obtain useful insights into the brain network connectivity. Advances in brain network analysis illustrates the brain as a dynamic interconnected network, capable of plasticity and adaptation.[18][19].

There are predominantly three types of network types that are used to investigate communication within the brain. **Structural Connectivity** analyses the physical connection of neurons among different regions of the brain. These are the anatomical network maps that indicate possible pathways that signals can travel in the brain. **Functional Connectivity** identifies brain regions which have similar frequency, phase or amplitude of correlated activity. This is typically carried out in various states of the brain, such as resting state or emotional processing to analyse enhanced connectivity between different regions of the brain for specialized activity. **Effective Connectivity**, in addition to analysing correlation between different regions of the brain, also determines the direction of information flow in the brain.

In this study, we attempt to verify if epilepsy leads to enhanced connectivity among various region of the brain. This is in fact, a first step towards understanding the role of communication networks in brain disorders. We use coherence of MEG data from the brain as a measure of connectivity, since connected regions seem to be synchronous, and can be quantified using coherence.

1.3.1 Related Works

There have been several studies in the past to correlate brain disorders with functional connectivity and coherence in the brain[20][21][22]. Ozerdam *et al.* [27] found that patients with bipolar disorder showed a diminished coherence in the gamma frequency region between frontal and temporal lobes. In Alzheimer's, a decrease in coherence is observed in alpha and beta bands between distant structures in resting state [26]. In schizophrenia, Yeragani *et al.*[28] found a decrease in sleep coherence in both beta and gamma frequency bands. Brazier [29] was the first to use coherence to detect the influence of one brain region over the other during epileptic discharge. Song *et al.* has shown that EEG coherence can be used to characterise a pattern of strong coherence in temporal lobe structures for epilpetic patients [30].

1.3.2 Contributions

- Using coherence as a measure of brain network connectivity, we establish an increase in connectivity among various regions of the brain during an epileptic discharge.
- We also propose a method to identify epilogenetic regions in the brain using network analysis. This method, when combined with existing methods for MRI coregistration and source localisation, makes a powerful visualisation tool.

CHAPTER 2

Generating Panorama from Fish-eye Images

2.1 Fish-eye Lens

Fish eye lens is an ultra wide angle lens producing strong visual distortion, intended to create a wide panoramic image. The term fish-eye was coined in 1906 by American physicist and inventor Robert Wood, based on how a fish sees the ultrawide hemispherical view of the sky from below water. There are two kinds of fish eye lenses used commercially : circular and full frame fish eye.

A circular fish eye camera takes a wide angle FOV image and inscribes this as a circle within the film frame. These have vertical, horizontal and diagonal FOVs of 180^o assuming a 180^o fish eye. Full-frame fish eye lenses enlarge the central part of the circular fish eye and fit it into a rectangular region. They have a diagonal FOV of 180^o. However, the horizontal and vertical FOVs are much less. For an equisolid angle type 15mm full-frame fisheye, the horizontal FOV will be 147^o and vertical FOV will be 94^o. Figure 2.1 shows an example for circular and full frame fish eye.

(a) Fish eye lens (b) Circular view (c) Full frame view

Figure 2.1: Fish eye camera lens

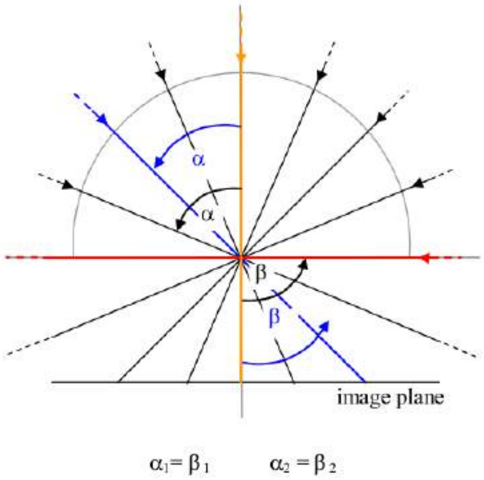

Figure 2.2: Central perspective projection model

2.2 Projection Model

Conventional cameras follow the central perspective projection algorithm to map the real world data to the image sensor plane. In this projection, the incident angle on to the camera sensor is equal to the outgoing angle. As seen from Figure 2.2, to realize a wide FOV for a conventional camera, either the screen size should be large or the distance of the screen from the aperture should be small. There are practical limits for both these parameters and hence realizing high FOVs is practically impossible. Let θ be the angle of incidence of a ray with the optical axis, f be the focal length of the camera and R be the distance of the image point from the center. Then the central perspective projection is given by

$$R = f.\tan(\theta) \tag{2.1}$$

From equation 3.2, it is clear that for an FOV of 180^o, the angle of incidence is 90^o and hence the the distance of the image point approaches ∞.

For fish eye projection, a ray incident at an angle of 90^o to the optical axis has to be mapped to a point at a finite distance from the image center. For this a different projection model becomes necessary. The fish eye projection model is based on the principle that in the ideal case, the distance between the image and the principle axis is a linear function of the angle of incidence. Hence a ray of light incident at 0^o gets

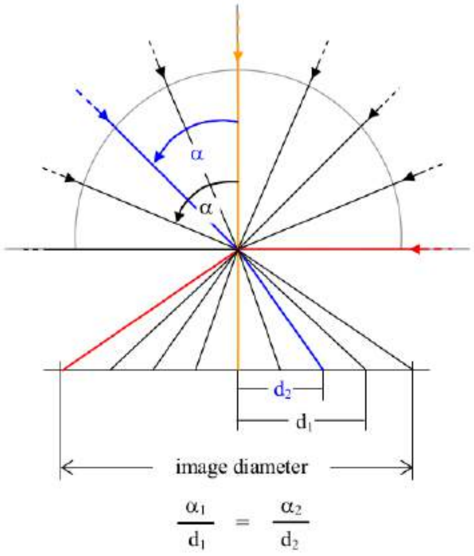

Figure 2.3: Fish eye projection model

mapped to the center of the circular image, while a ray incident at 90^o gets mapped to the periphery of the circular region. As seen in Figure 2.3, the rays incident on the lens in refracted towards the principle axis. This is achieved by the types and configuration of the lenses of a fish eye lens system. A summary of the various projection models used by fish eye lens system is shown in Table 2.1. In our algorithm we follow the equidistant projection model

Projection Model	**Math**	**Real Lenses**
Equidistant	$R = f.\theta$	e.g. Peleng 8mm f/3.5 Fisheye
Stereographic	$R = 2f.\tan(\frac{\theta}{2}$	e.g. Samyang 8 mm f/3.5
Orthographic	$R = f.\sin(\theta)$	e.g. Yasuhara - MADOKA 180 circle fisheye lens
Equisolid	$R = 2f.\sin(\frac{\theta}{2}$	e. g. Sigma 8mm f/4.0 AF EX
Thoby fisheye	$R = k_1.f.\sin(k_2.\theta)$	e. g. AF DX Fisheye-Nikkor 10.5mm f/2.8G ED

Table 2.1: Fish eye projection models

2.3 Algorithm

In this section, an algorithm to convert a given fish eye image to equirectangular projection is discussed. For the development of this algorithm, it is assumed that a circular image is converted to a square image. We use inverse mapping to tranform the image which is a common method used in image transformation. In inverse mapping, for each pixel of the output image, the corresponding pixel value in the input fish-eye image is

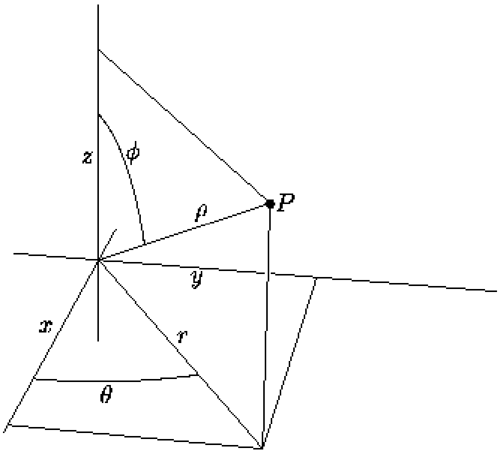

Figure 2.4: 3D coordinate system

computed. Here we discuss the transformation used to map rectiliner coordinates to fish-eye coordinates.

In spherical coordinate system, the 3D world can be defined by the parameters (z, θ, ϕ). θ corresponds to the angle of a point in the horizontal direction and varies from $-\pi$ to π. ϕ corresponds to the angle the point makes in the vertical direction and varies from $-\pi/2$ to $\pi/2$ (Figure 2.4). Let I_r represent the rectilinear image and I_f represent the fish-eye image. Let (i_r, j_r) represent the coordinates in the rectilinear space (row number, column number). Let the rectilinear image be of dimensions $M \times M$. The rectilinear image of a 360^o degree encompasses the whole 3D space. Hence the coordinates can be transformed into corresponding angle as follows:

$$\begin{aligned} \theta &= \pi(\frac{j_r}{M}) \\ \phi &= \pi(\frac{i_r}{M}) \end{aligned} \tag{2.2}$$

For an equidistant image, z can be taken as constant. Here we assume z to be 1.

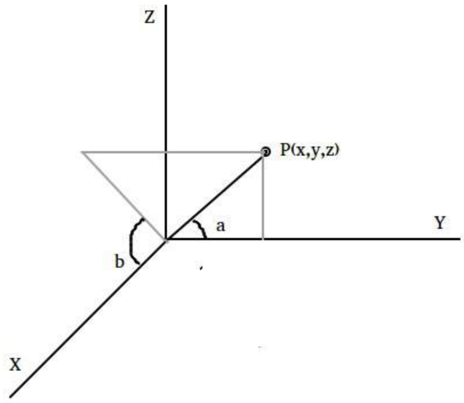

Figure 2.5: Angles made by the line connecting 3D point and the center to X-Y plane and X axis

Then corresponding 3D points can be written as

$$\begin{aligned} x &= \sin(\phi).\cos(\theta) \\ y &= \sin(\phi).\sin(\theta) \\ z &= \cos(\phi) \end{aligned} \tag{2.3}$$

Let us define angle a and b as shown in Figure 2.5. a is the angle made by the line connecting the 3D point to the centre and the horizontal plane, while b is the angle made by the projection of the line with the X axis. It is to be noted that a represents the angle at which a ray is incident on the fish eye camera aperture.

$$\begin{aligned} a &= \tan^{-1}(\frac{\sqrt{x^2+z^2}}{y}) \\ b &= \tan^{-1}(\frac{z}{x}) \end{aligned} \tag{2.4}$$

In the equidistant projection system for fish eye images, the distance of an image point from the centre is proportion to the angle of incidence of a ray. Following this model, we can define r as,

$$r = M.\frac{a}{FOV} \tag{2.5}$$

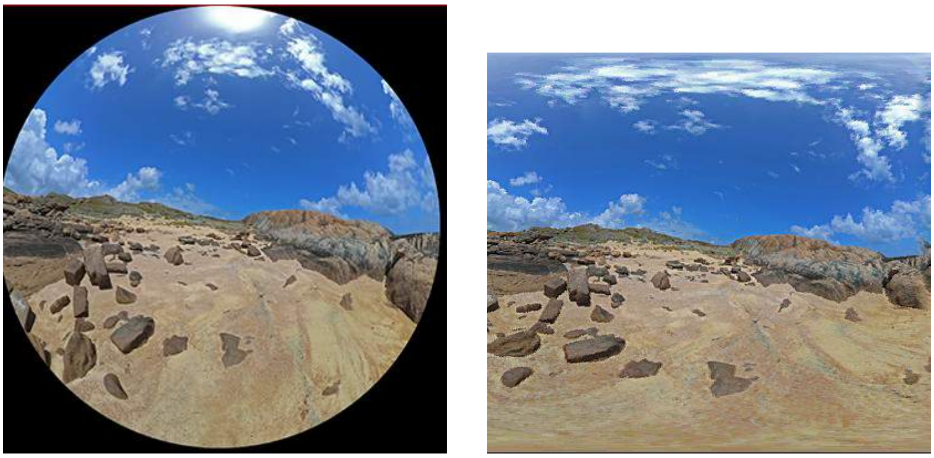

(a) Fish-eye image (b) Rectilinear Image

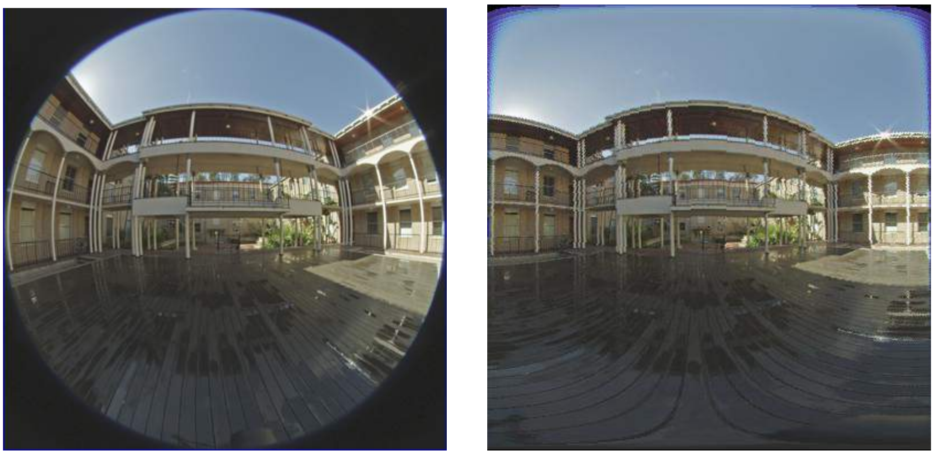

(c) Fish-eye Image (d) Rectilinear Image

Figure 2.6: Fisheye to rectilinear transformation. (a)-(b) Transformation for an FOV of 210^o. (c)-(d) Transformation for an FOV of 180^o

Here, a represents the angle of incidence and FOV is the Field-of-View of the fish eye camera. Finally, the coordinates in the fish-eye domain can be represented as

$$\begin{aligned} i_f &= 0.5M + r.sin(b) \\ j_f &= 0.5M + r.cos(b) \end{aligned} \tag{2.6}$$

Figure 2.6 shows some examples of the algorithm. The two image pairs in the example shown corresponds to FOV of 210^o and 180^o respectively. In the second pair, barrel distortion induced by the fish eye camera is clearly visible in the vertical parts of the building. Our algorithm rectifies this distortion as is evident from the straight pillars of the rectified image. Since our algorithm assumes equiplanar scene, a distortion is observed in parts closer to the camera. However, for a full-frame fish eye, this problem

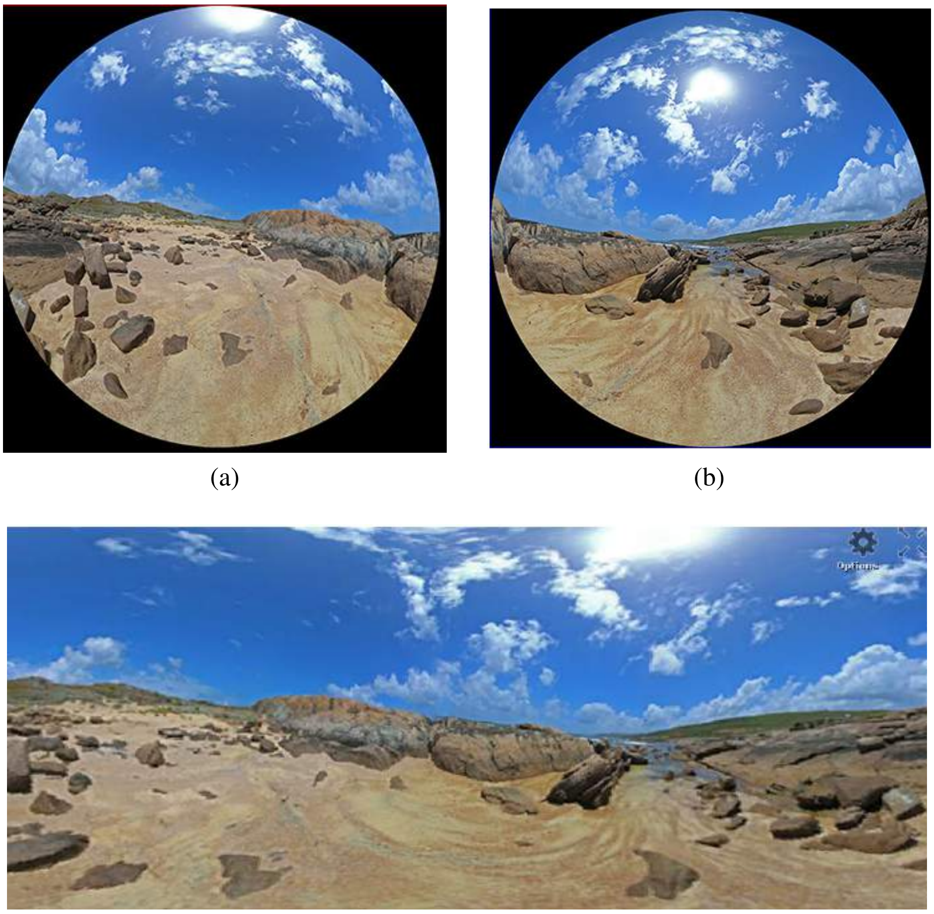

(a) (b)

(c) Panorama

Figure 2.7: Panorama Generation (a)-(b) Pair of fish eye images. (c) The 360^o panoramic image

is of no significance as only the central part of the image is displayed there.

2.4 Panorama

Two back-to-back aligned fish-eye cameras are required to generate 360^o panoramic images. Conventional panorama generation algorithms require one to match feature points using algoirthms such as SIFT, and then a homography estimation to generate the panorama. However, for this problem, we can take advantage of the inherent alignement of the camera system. Hence the panoramic image can easily be obtained by stitching the two final output images. A histogram normalization may be performed to account for lighting differences in indoor scenes. Figure 2.7 shows an example of generating panorama from 2 images. The individual images correspond to a FOV of 210^o and hence the uncropped panoramic image corresponds to a horizontal FOV of 420^o.

2.5 Conclusions

In this chapter, generation of full view panoramic image from a pair of fish-eye lenses is discussed. Fish-eye lenses are wide angle lenses which are capable of capturing images with FOV greater than 180^o. However this added flexibility comes with the cost of heavy barrel distortion by virtue of the fish eye projection technique. We illustrate an algorithm which can correct these distortions to project the fish eye image back to the rectilinear plane. It requires only the knowledge of FOV and informtation on other camera parameters and calibration is not needed. There is scope for improvement in the image stitching process. Also, the algorithm could be extended to process incoming video stream in real time. This would be useful for application such as self-driving cars.

CHAPTER 3

Super Resolution with Motion Artefacts

3.1 Image Formation Model

3.1.1 Classical Super-Resolution

We first briefly review the super-resolution model without image degradations and subsequently develop an acquisition model for images with RS and MB artefacts. Let $\mathbf{U}$ represent the required HR image of dimensions $sP \times sQ$, where s is the super-resolution factor, and P and Q represent the dimensions of the LR image. Let $\mathbf{u}$ represent the lexicographically ordered image vector of size $s^2PQ \times 1$. Let $\boldsymbol{\mathcal{H}}$ be a warping matrix of dimensions $s^2PQ \times s^2PQ$ which multiplies $\mathbf{u}$ to produce a warped latent image. In the absence of RS-MB artefacts, each of the LR image is a manifestation of a single warp on the original HR image $\mathbf{u}$. Hence each row of $\boldsymbol{\mathcal{H}}$ contains a maximum of four non-zero entries corresponding to the bilinear interpolation coefficients obtained on application of the warp at a given pixel location. Let $\mathbf{D}$ be the decimation matrix which multiplies the warped HR image vector to produce the observed LR image vector $\mathbf{v}$ of dimensions $P \times Q$. The decimation matrix is of dimensions $PQ \times s^2PQ$ and it downsamples an HR image into its LR correspondence. Then the super-resolution problem in the absence of RS-MB artefacts can be formulated as

$$\mathbf{v} = \mathbf{D}\boldsymbol{\mathcal{H}}\mathbf{u} \tag{3.1}$$

The principle of multi-image super resolution is illustrated in Figure 3.1.

3.1.2 Super-Resolution with camera motion

Consider image acquisition in the global shutter case. Let $\boldsymbol{\mathcal{T}}$ be the trajectory followed by the GS camera during the exposure time interval $\mathrm{t_e}$. The image produced by the

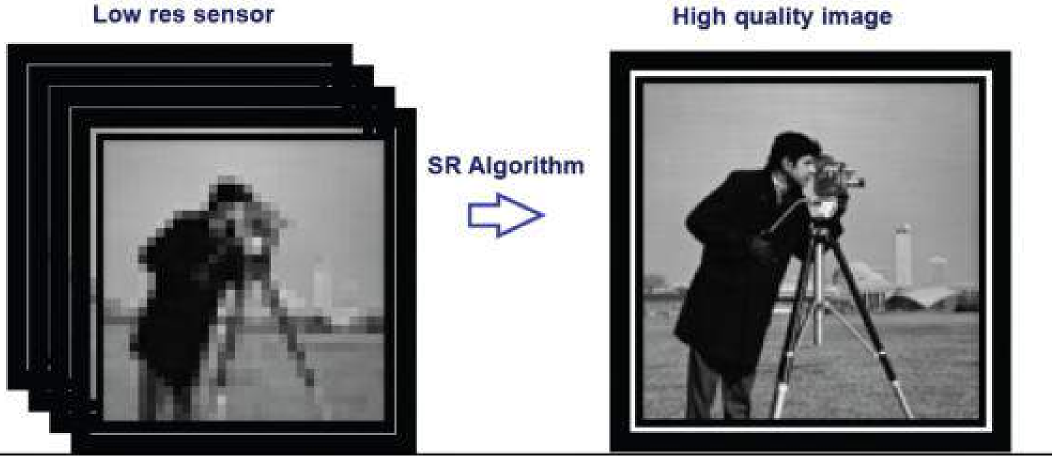

Figure 3.1: Multi-image super resolution. An HR image of SR factor s can be obtained from s LR images. Each image adds extra information by virtue of its motion, which can be captured to form the HR image

camera will be the average of the images seen by the camera during $\mathbf{t_e}$. This can be formulated as

$$\mathbf{g} = \frac{1}{t_e} \int_{0}^{t_e} \boldsymbol{\mathcal{H}}_{\boldsymbol{\mathcal{T}}(t)} \mathbf{u} dt \tag{3.2}$$

where $\boldsymbol{\mathcal{H}}_{\boldsymbol{\mathcal{T}}(t)}$ denotes the warping matrix of the trajectory at the time instant t and $\mathbf{g}$ is the image vector for global shutter camera motion.

In the case of rolling shutter cameras, all the rows do not get exposed simultaneously as in the case of GS. Instead, there is an inter-row delay of β between the exposure start times of subsequent rows. As a result, each row gets exposed to different parts of the whole camera trajectory, even though the row exposure time, α is the same for all the rows. Hence each row has to be treated as a separate GS case. Let $\mathbf{r_i}$ and $\mathbf{u_i}$ be the vectors corresponding to the i^{th} rows in the rolling shutter affected image, $\mathbf{R}$, and $\mathbf{U}$ respectively. Then,

$$\mathbf{r_i} = \Big(\frac{1}{\alpha} \int_{t_i}^{t_i+\alpha} \boldsymbol{\mathcal{H}}_{\boldsymbol{\mathcal{T}}(t)} \mathbf{u} dt \Big)_i \tag{3.3}$$

Here t_i the time at which the row i begin to get exposed and α is the row exposure duration. Also,

$$t_i = (i-1) \times \beta \tag{3.4}$$

For practical purposes, the continuous trajectory can be approximated as a set of distinct poses along the trajectory. We define $\boldsymbol{\mathcal{P}}$ as the discreet pose space over the whole trajectory, and $\boldsymbol{\mathcal{P}_i}$ as the poses row i is exposed to. Then,

$$\mathbf{r_i} = \frac{1}{A} \sum_{p \in \boldsymbol{\mathcal{P}_i}} \boldsymbol{\mathcal{H}}_p \mathbf{u_i} \tag{3.5}$$

where A is the number of discreet poses within the row exposure time, α and $\boldsymbol{\mathcal{H}}_p \mathbf{u_i}$ is the warping matrix corresponding to the pose p. The warping matrix for the complete RS image can be represented as $\mathbf{H}(\boldsymbol{\mathcal{P}})$, where $\mathbf{H}$ is a function of $\boldsymbol{\mathcal{P}}$. Hence, the complete image model for super-resolution in the presence of camera motion as,

$$\mathbf{v} = \mathbf{DH}(\boldsymbol{\mathcal{P}})\mathbf{u} \tag{3.6}$$

$\mathbf{H}(\boldsymbol{\mathcal{P}})$ contains at most $4A$ non zero entries per row. $\mathbf{H}(\boldsymbol{\mathcal{P}})$ represents an average of sPA distinct poses. The image formation for GS and RS cases are illustrated in figure 3.2.

3.2 Optimization Problem

3.2.1 Objective Function

Consider the set of observed LR image vectors $\{\mathbf{i_k}\}$, where $k = \{1, 2, ..., 2s\}$. The HR image vector $\mathbf{u}$ is to be estimated from these images. From equation 3.6, the objective function can be written as,

$$\min_{\mathbf{u}, \mathcal{P}_\mathbf{k}} \sum_{k=1}^{s^2} ||\mathbf{DH}(\boldsymbol{\mathcal{P}}_\mathbf{k})\mathbf{u} - \mathbf{v_k}||_2^2 + \alpha \mathbf{u}^T \mathbf{L} \mathbf{u} \tag{3.7}$$

Here $\boldsymbol{\mathcal{P}_k}$ denotes the camera motion trajectory for the k^{th} image. The second term in the equation is a regularization term with positive constant value α. $\mathbf{L}$ is the discrete form of variational prior, which is a positive semi-definite block tridiagonal matrix constructed of values depending on the gradient of $\mathbf{u}$. If the camera trajectory is known, $\mathbf{H}(\boldsymbol{\mathcal{P}}_\mathbf{k})$ can be estimated easily, and this becomes an example of non-blind super resolution. Figure 3.3 shows an example of non-blind multi image SR. Once one LR image

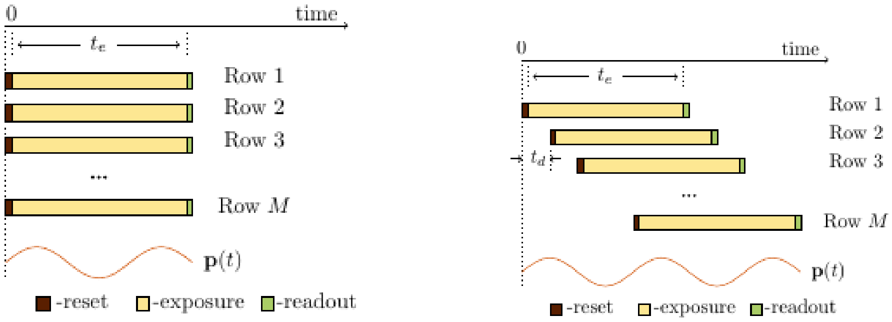

(a) Scanlines for GS (b) Scanlines for RS

(c) GS image (d) RS image

Figure 3.2: Illustration of image formation in camera (a) GS acquisition. It can be seen that β is zero and hence all rows are exposed simultaneously. (b) RS acquisition. Different rows begin exposure at different times due to non-zero β. By varying α/β, the amount of MB and RS can be adjusted. (c) Image with motion blur alone (d) Image with both MB and RS (Image Courtesy (a) and (b) [15]

is shown here for ease of comparison. The LR images were generated synthetically.

In blind super resolution, the trajectory information is missing, and it has to be estimated along with the latent HR image. The estimation of $\mathbf{u}$ and $\mathcal{P}_k$ simultaneously is a heavily ill-posed problem. Hence we follow the Alternating Minimization(AM) strategy. In AM, we alternate between the estimation of $\mathbf{u}$ and $\mathcal{P}_k$ in subsequent iterations assuming separate convex optimization problems. Starting with an initial estimate of the image $\mathbf{u_0}$, we estimate the trajectory $\boldsymbol{\mathcal{P}_{k_1}}$ and the process is continued till convergence. This process is elaborated below.

3.2.2 Trajectory Estimation

Following the work of Su *et al*[17], we model the camera motion as a polynomial trajectory. From the analysis of 40 publicly available camera trajectory datasets by Kohler


(a) Input LR image (b) Output HR image

Figure 3.3: Synthetic result for non-blind SR, where image trajectory is known beforehand. A PSNR of 31 was obtained in this case. The algorithm was run for 10 iterations

et al[16], it was observed that the camera motion trajectory can be modelled by 3^{rd} or 4^{th} order polynomial. Figure 3.4 shows camera motion for trajectory 1 in the kohler database, and its approximation by a 4^{th} order polynomial. Hence a camera motion trajectory can be written as

$$\boldsymbol{\mathcal{P}} = a_0 + a_1 t + a_2 t^2 + a_3 t^3 + a_4 t^4 \tag{3.8}$$

Let $\theta_{\mathbf{k}}$ denote the set of polynomial coefficients corresponding to the k^{th} image. Now equation 3.7 reduces to

$$\min_{\mathbf{u},\theta} \sum_{k=1}^{s^2} ||\mathbf{DH}(\theta_{\mathbf{k}})\mathbf{u} - \mathbf{v_k}||_2^2 + \gamma \mathbf{u}^T \mathbf{Lu} \tag{3.9}$$

For a general camera motion, the trajectory consists of motion in 6 dimensions, 3 translational motions and 3 rotational motions $(t_x, t_y, t_z, r_x, r_y, r_z)$ where, z is the camera axis. However the 6D camera trajectory can be approximated by a 3D motion (t_x, t_y, r_z) or (r_x, r_y, r_z) for an approximately planar scene, or a scene with less depth variations. We use the trajectory set (t_x, t_y, r_z) for our experiments. Hence the problem of warp estimation reduces to the estimation of 15 polynomial coefficients, assuming a 4^{th} order polynomial trajectory for each dimension.

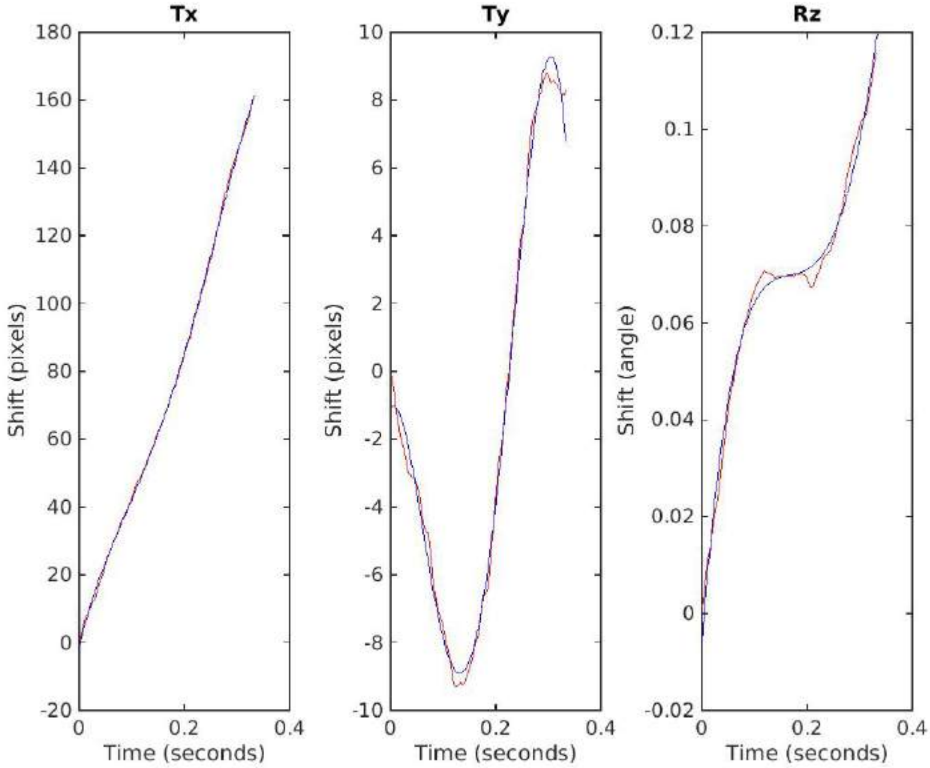

Figure 3.4: Approximation of camera motion trajectory by a 4^{th} order polynomial for an exposure duration of $\frac{1}{3}$ seconds. The red curve shows the real trajectory from Kohler database and the blue curve shows its approximation by a polynomial for translation in horizontal and vertical directions and rotation along camera axis.

Following equation 3.9, the estimation of θ_k for the j^{th} iteration can be written as,

$$\theta_{\mathbf{k}}{}^{j} = \arg\min_{\theta_{\mathbf{k}}} ||\mathbf{DH}(\theta_{\mathbf{k}})\mathbf{u}_j - \mathbf{v_k}||_2^2 \tag{3.10}$$

where $\mathbf{u}_j$ is the HR image estimated from the j^{th} iteration. $\mathbf{H}(\theta_{\mathbf{k}})$ can be estimated with the assumption of polynomial trajectory and the knowledge of exposure parameters α and β.

This non-linear least squares problem can be solved using Gauss-Newton method. In each iteration, this algorithm updates $\theta_{\mathbf{k}}$ as follows

$$\theta_k^{j+1} = \theta_{\mathbf{k}}{}^{j} + \Delta\theta \tag{3.11}$$

$\Delta\theta$ is determined as below

$$\Delta\theta = (\mathbf{J^T J})^{-1}\mathbf{J^T}(\mathbf{DH}({\theta_{\mathbf{k}}}^{j})\mathbf{u}_j - \mathbf{v_k}) \tag{3.12}$$

where $\mathbf{J}$ is the Jacobian of the vector $(\mathbf{DH}({\theta_{\mathbf{k}}}^{j})\mathbf{u}_j - \mathbf{v_k})$. Let

$$\mathbf{v_{est}}(k, \boldsymbol{\theta}) = \mathbf{DH}(\boldsymbol{\theta})\mathbf{u}_j - \mathbf{v_k} \tag{3.13}$$

Then,

$$\mathbf{J} = \lim_{\mathbf{h}\to 0} \frac{\mathbf{v_{est}}(k, \boldsymbol{\theta_k} + \boldsymbol{h}) - \mathbf{v_{est}}(k, \boldsymbol{\theta_k})}{\boldsymbol{h}} \tag{3.14}$$

3.2.3 HR Image Estimation

Once the trajectory coefficients are estimated, we use equation 3.7 to estimate the HR image for the $j + 1^{th}$ iteration.

$$\mathbf{u}^{j+1} = \arg\min_{\mathbf{u}} \sum_{k=1}^{s^2} ||\mathbf{DH}(\boldsymbol{\mathcal{P}}_{\boldsymbol{k}}^{j})\mathbf{u} - \mathbf{v_k}||_2^2 + \gamma\mathbf{u}^T\mathbf{Lu} \tag{3.15}$$

For simplicity, we denote $\mathbf{H}(\boldsymbol{\mathcal{P}}_{\boldsymbol{k}}^{j})$ by $\mathbf{H_k}$. To solve equation 3.15, we differentiate the right hand side of the equation w.r.t $\mathbf{u}$ and set the value to zero to obtain

$$\sum_{k=1}^{s^2} {\mathbf{H_k}}^T\mathbf{D}^T\mathbf{DH_k u} + \gamma\mathbf{Lu} = \sum_{k=1}^{2s} {\mathbf{H_k}}^T\mathbf{D}^T\mathbf{v_k} \tag{3.16}$$

The matrix $\mathbf{D}$ spreads intensity equally to s^2 pixels in the LR image. The matrix $\mathbf{H_k}$ is the warping function to produce the required RS image. We use a constant value of α based on visual assessment. We use the method of conjugate gradients (*pcg* in Matlab R2014b) to solve the above equation.

3.3 Initial Estimates

By alternating through the image subspace and trajectory subspace, the AM algorithm is guaranteed to hit a local minimum. However, due to the heavily ill posed nature of the problem, particularly due to the presence of RS effect, this local minimum may not be the required HR image. Hence a good initial estimate of the trajectory coefficients or the latent HR image is required to kick start the AM sequence. In this chapter, we examine the use and viability of using initial estimates.

3.3.1 Initial Trajectory Coefficients

In this section, we demonstrate the power of a good initial estimate on the trajectory on the final image estimate. In figure 3.5 the algorithm is initialized with a zero image and the original trajectory coefficients. The input to the algorithm is five LR images degraded by RS and MB. The figure also shows the same example where the algorithm is initialized with a zero image, but the initial trajectory coefficients are offset by 90% from the actual value. It is evident from the illustrations that the result of the algorithm is heavily dependent on the initial estimates.

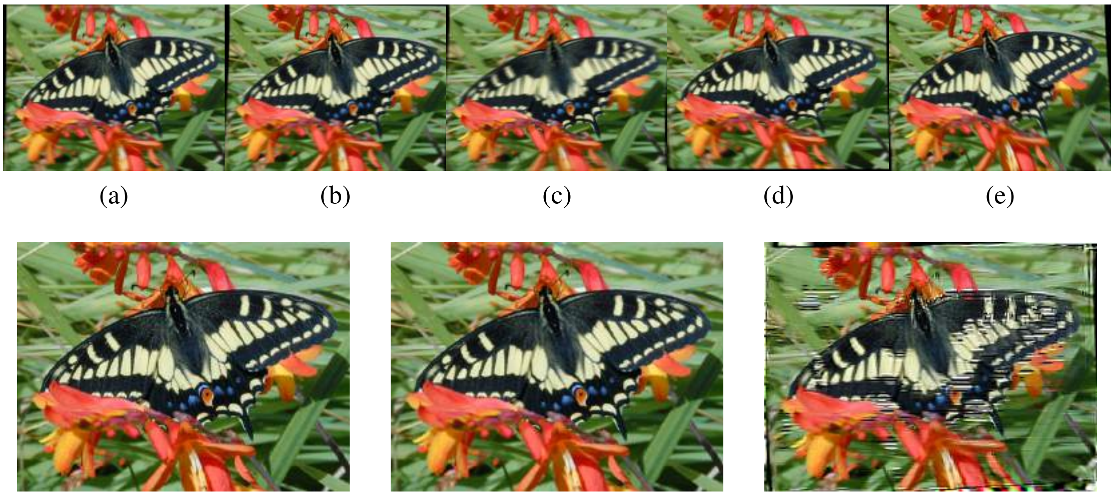

(a) (b) (c) (d) (e)

(f) Original Image (g) Output with good estimates (h) Output with poor estimates

Figure 3.5: Synthetic result for blind SR with initial trajectory estimates. (a) - (e) shows the input LR images. (f) Original Image (g) Estimated image after 7 iterations for good initial trajectory estiation. The algorithm converges with a PSNR of 33.42 (h) Estimated image after 10 iterations for poor initial estimates. Here the algorithm fails to produce a good HR estimate

3.3.2 Initial Image Estimation

Getting a good initial estimate for camera motion trajectory is not always feasible. In this section, we examine the algorithm with initial image estimate. For *Estimating initial images alone*, we assume that the image is locally free of RS effect. We partition the image into smaller non-overlapping image patches which are assumed to be free of RS effect. Also the motion blur is assumed to be space invariant foe each of the image patches (again, for initialisation purposes only). We now use multichannel blind deconvolution (MCBD) method outlined by Sroubek *et al.* [citiation]on the LR image patches to obtain HR image patches. The resulting HR images are then combined back to obtain the initial HR image estimate. Figure 3.6 shows an example of an LR patch super resolved using MCBD.

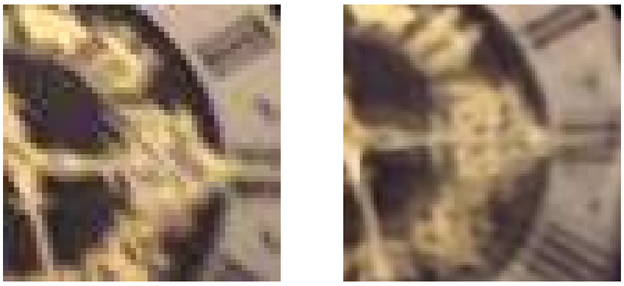

(a) LR Patch (b) HR Patch

Figure 3.6: Result of Sroubek's MCBD algorithm. The algorithm is run for 10 iterations to obtain an initial estimate

Since the distorted image is a convolution of the HR image matrix with warping matrix, a translated HR image matrix convolved with a translated warping matrix also produces the same LR image. However, a small global translation in the x or y direction is admissible if an undistorted HR image is obtained. An overview of the SR algorithm is given in algorithm 1. Figure 3.7 shows an illustration of the algorithm graphically.

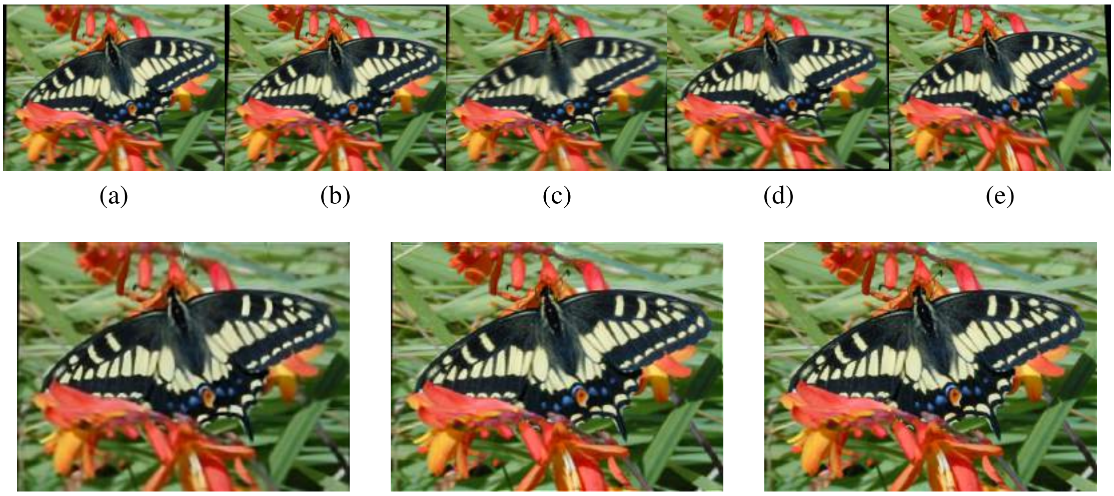

(a) (b) (c) (d) (e)

(f) Initial Image Estimate (g) Estimated HR image after 1 iteration (h) Estimated HR image after 150 iterations

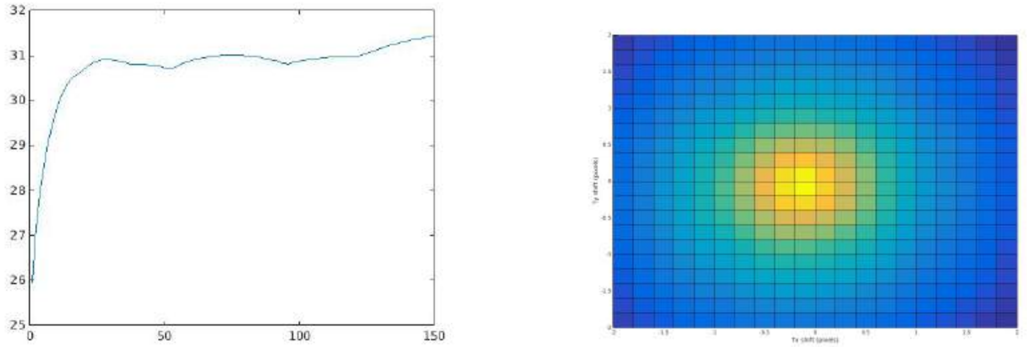

(i) PSNR plot (j) Shift map

Figure 3.7: Synthetic result for blind SR with initial image estimate.(a) - (e) Input LR images. (i) The plot of PSNR as a function of iterations. It can be seen that the PSNR improves consistently as the algorithm proceeds (j) The shift map, which shows the translation in the image. Highest PSNR is obtained for a shift of approximately 0.4 pixels. The PSNR plot is plotted for the highest PSNR obtained in the image.

Algorithm 1 Overview of the SR Algorithm

```
Input $s$ images
Execute patch-wise multichannel deconvolution to obtain initial image
while No. of iterations/convergence do
    Estimate trajectory coefficients $\boldsymbol{\theta_k}$
    Estimate HR image $\boldsymbol{u}$
end
```

3.4 Experimental Results

In this chapter, some more examples of our algorithm is provided along with comparisons with state-of-the-art SR methods.

3.4.1 Synthetic Examples

Figures 3.8 and 3.9 shows synthetic examples with synthetic trajectories. Parameter values of $\alpha = 100$ and $\beta = 1$ were used for the experiments. The extracted image patch clearly shows the SR algorithm in action. A sufficiently good PSNR was observed for all the experiments, and the outputs are visually pleasing with a shift within acceptable boundaries. The estimate trajectories look structurally same with the ground truth trajectories, with a slight shift.

Figure 3.10 shows an example of a synthetic example on a real trajectory. The trajectories are obtained from Kohler's database which captures actual handshakes of 6 subjects. The parameter values of $\alpha = 100$ and $\beta = 1$ is used for generating RS images as earlier. We used a row exposure time of $1/20$ seconds for our experiments. The trajectory is estimated with a second order a polynomial in this example, and produces remarkable results with a PSNR of 30.88.

3.4.2 Comparisons

We compare our algorithm with state of the art SR algorithms. We consider only those methods which take into account the camera motion during the capture. Our algorithm is compared with the multi-channel blind deconvolution algorithm by Sroubek et.al in figure 3.11. It can be seen that, our algorithm significantly outperforms the other algorithms for all the cases.

(a) (b) (c) (d) (e)

(f) Ground truth image (g) Initial image estimate (h) Estimated HR image

(i) LR patch (j) Est. HR patch

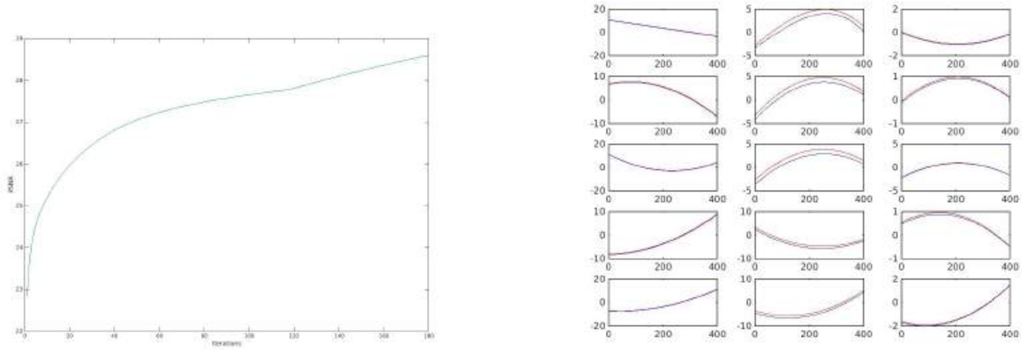

(k) PSNR plot (l) Trajectory Estimation

Figure 3.8: Synthetic example for $\alpha = 100, \beta = 1$.(a) - (e) Input LR images. (k) The plot of PSNR as a function of iterations. A PSNR of 29 is observed for this case (l) Comparison of ground truth trajectory with estimated trajectory as a function of number of poses. The red curve represents ground truth and the blue curve represents estimates trajectory. Columns represent Tx, Ty and Rz respectively while rows represent the 5 input images

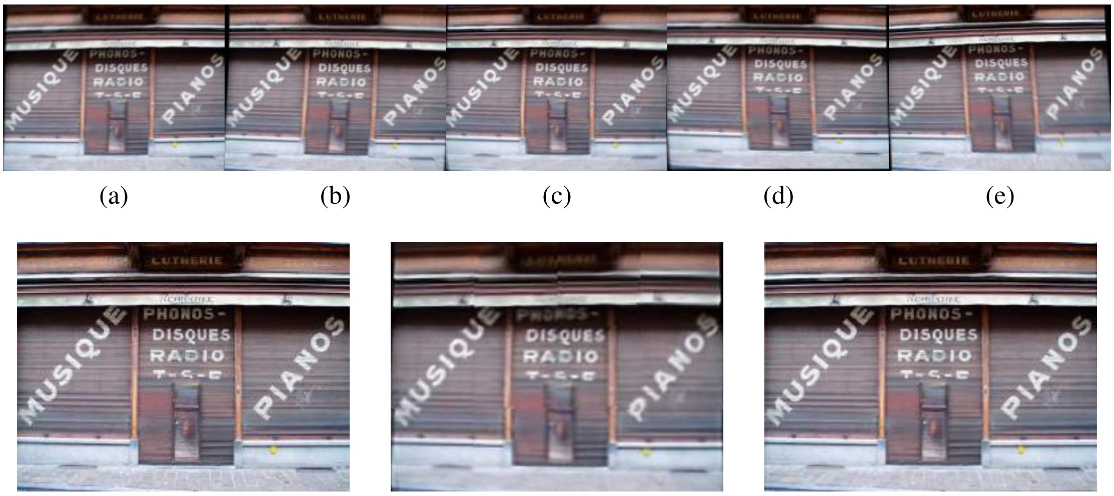

(a) (b) (c) (d) (e)

(f) Ground truth image (g) Initial image estimate (h) Estimated HR image

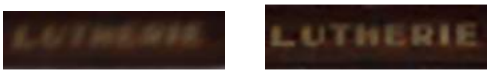

(i) LR patch (j) Est. HR patch

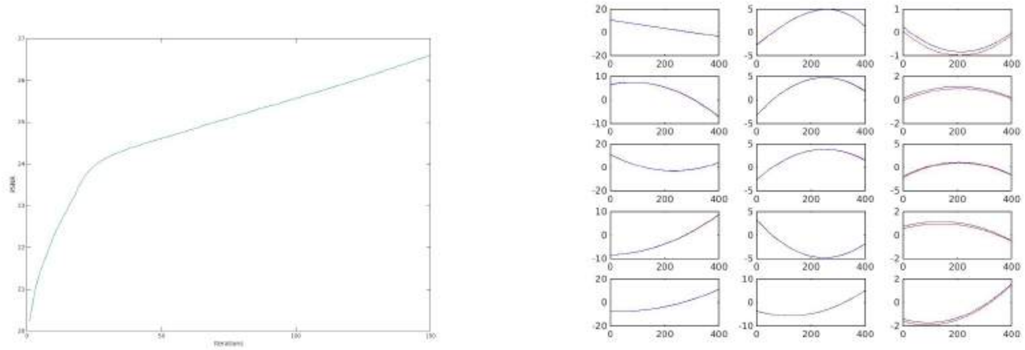

(k) PSNR plot (l) Trajectory Estimation

Figure 3.9: Synthetic example for $\alpha = 100, \beta = 1$.(a) - (e) Input LR images. (k) The plot of PSNR as a function of iterations. A PSNR of 27 is observed for this case (l) Comparison of ground truth trajectory with estimated trajectory as a function of number of poses. The red curve represents ground truth and the blue curve represents estimates trajectory. Columns represent Tx, Ty and Rz respectively while rows represent the 5 input images

(a) (b) (c) (d) (e)

(f) Ground truth image (g) Initial image estimate (h) Estimated HR image

(i) LR patch (j) Est. HR patch

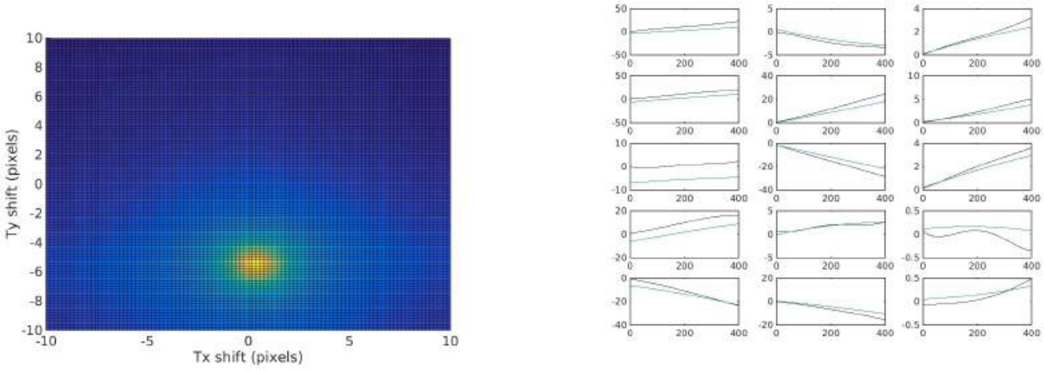

(k) Shift map (l) Trajectory Estimation

Figure 3.10: Synthetic example for $\alpha = 100, \beta = 1$.(a) - (e) Input LR images. (k) The shift plot for the example. A translational shift of around 5 pixels is observed for maximum PSNR, which is 30.88 (l) Comparison of ground truth trajectory with estimated trajectory as a function of number of poses. The black curve represents ground truth and the blue curve represents estimates trajectory. Columns represent Tx, Ty and Rz respectively while rows represent the 5 input images

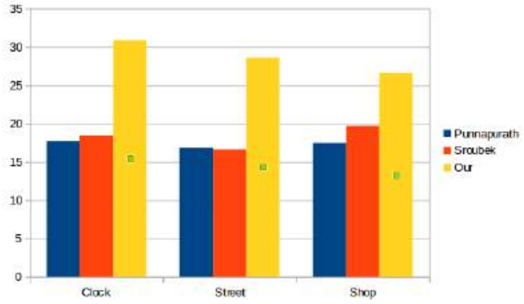

(a)

(b) Ground Truth (c) Sroubek (d) Punnapurath (e) Our

(f) Ground Truth (g) Sroubek (h) Punnapurath (i) Our

(j) Ground Truth (k) Sroubek (l) Punnapurath (m) Our

Figure 3.11: Comparison with state of the art super resolution techniques. (a) Our results are compared with MCBD algorithm by Sroubek et.al. Our algorithm is superior since MCBD is unable to handle RS effects and space varying blur. (b) - (m) shows the corresponding images for the all the algorithms

3.5 Conclusions

In this chapter, we presented the problem of multi-image super resolution in the presence of camera motion. Classical super resolution algorithms are designed for stationary cameras. With the advance of mobile cameras, the assumption of stationary camera becomes obsolete and algorithms which takes into account the handshake during camera exposure becomes essential. We developed an algorithm which can handle the motion blur due to camera motion as well as the rolling shutter effect observed in CMOS sensor cameras used in smartphones. We propose a model in which we alternate between the estimation of the super resolved image and the camera trajectory during the exposure. The camera trajectory is modelled as a polynomial and experiments on Kohler database show that common handshake motion can be approximated by a polynomial of degree at most four. Once the trajectory is known, latent image can be estimated given the knowledge of row exposure duration and inter-row delay times, which are defined in section 3.1.2. We also showed the effects of initial estimates on the quality of the final image and derived a method for image initialisation. Our results are compared with some of the state of the art super resolution techniques and our algorithm produces images which are visually and quantitatively acceptable. We used PSNR of between estimated and ground truth images as a quantitative measure.

As an extension of the problem, learning based methods could be explored for camera motion estimation, which would produce a boosted performance in speed, once the training is over. Also algorithms which remove the dependency on the camera exposure parameters can also be explored.

CHAPTER 4

Analysis of MEG Data for Subjects with Drug-Resistant Epilepsy

4.1 Coherence Analysis of MEG Data

4.1.1 Magnetoencephalography

Magnetoencephalography (MEG) is a non-invasive functional neuro-imaging technique, which measures the magnetic fields associated with primary intracellular currents in the brain. A majority of MEG signals are caused by excitatory postsynaptic potentials, due to the flow of ions into the postsynaptic dendritic membranes of the apical dendritic pyramidal cells. For a detectable MEG signal outside the scalp, approximately 1 million non-radially symmetric, spatially aligned neurons are synchronously activated, and they produce an externally observable magnetic field, which generates about a 100-fT magnetic field[23]. A magnetically sealed room is essential for MEG measurement due to strong external magnetic interference. The pyramidal cells are located near the surface of the scalp. Due the attenuation of magnetic signals, a clinically useful method for measuring deep brain (non-cortical) MEG signals is still unavailable.

Although, MEG and EEG signals originate from the same neuro-physiological processes, there are important differences. Magnetic fields are less distorted than electric fields by the skull and the scalp, which results in better spatial resolution in MEG. Also, the decay of magnetic fields as a function of distance is more pronounced than for electrical fields. Hence, MEG is more sensitive to superficial cortical activity, which makes it useful for the study of neocortical epilepsy.

Data Acquisition

30 seconds of MEG data was obtained from a patient with drug-resistant epilepsy for epileptic and resting cases(Courtesy of Dr. Jyotirmoy, NBRC, Gurgaon). Interference caused by external and nearby sources is suppressed from the data using tSSS artefact reduction method[24]. A sampling rate of 1 kHz was used for the acquisition, and the signal was low-pass filtered to 70 Hz, since most of the clinically relevant brain activities occur in this region. The MEG data was analysed using the MNE package provided by python. A screenshot of the acquired MEG for epileptic and non - epileptic case for a patient is provided in Figure 4.1.

4.1.2 Coherence Analysis

Coherence is a mathematical technique that quantifies the frequency and amplitude of the synchronization of neuronal patterns of oscillating brain activity. Coherence is an estimate of the consistency of relative amplitude and phase between signals detected in coils or electrodes within a set frequency band. In sensor space, if signals are in phase then their amplitudes will add, if they are out of phase the signals will subtract possibly reducing the coherence value. In source space, the amplitude of the underlying source can be used to determine the strength of the connectivity.

Coherence is a linear math method in the frequency domain for calculating neuronal networks. The result is a symmetrical matrix that provides no information on directionality. Coherence is the most common measure used to determine if different areas of the brain are generating signals that are significantly correlated(coherent) or not significantly correlated (not coherent). Coherence is preferred over time domain analysis such as correlation due to its superior tolerance to noise in the data, since MEG signals are highly prone to external magnetic noise.

Strictly speaking coherence is a statistic that is used to determine the relationship between two data sets (i.e. coils or electrodes). It is used to determine if the signal content of two inputs are the same or different. If the signals measured by two electrodes or coils are identical then they have a coherence value of 1; depending on how dissimilar

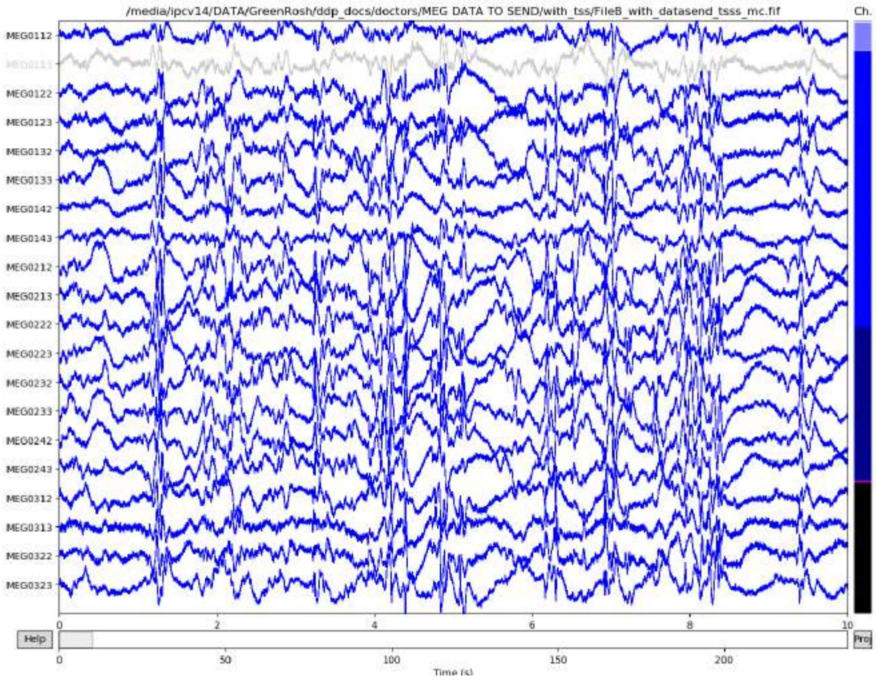

(a) MEG data with epilepsy

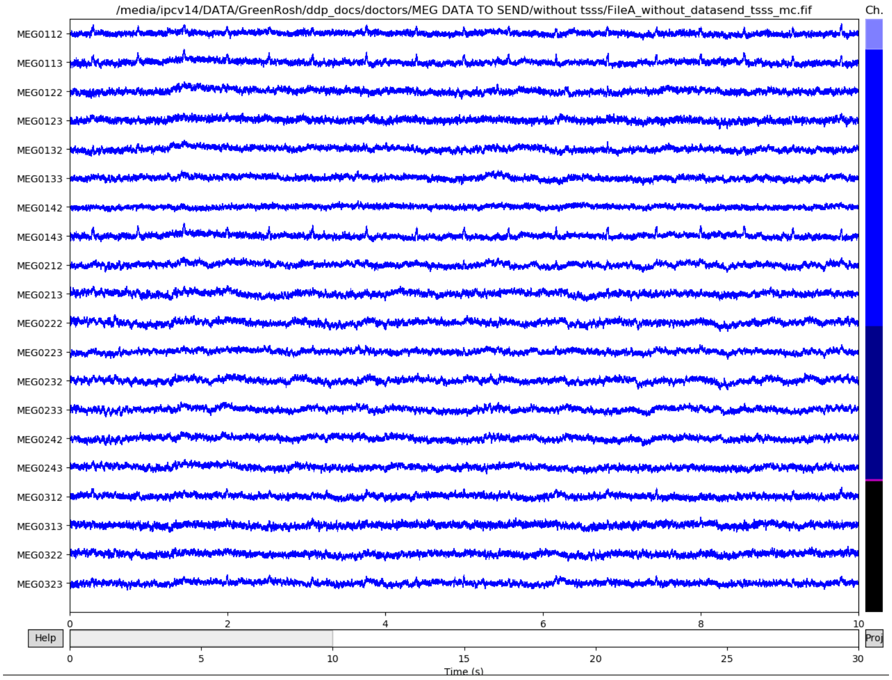

(b) MEG data without epilepsy

Figure 4.1: MEG data for epileptic and resting state

they are the coherent value will approach 0.

Let x and y be the two signals whose coherence is to be estimated. Let S_{xx} and S_{yy} be the power spectral densities(PSD) of the signals x and y. Let S_{xy} be the cross spectral density of the two signals. We define the coherence between the two signals, γ_{xy} as,

$$\gamma_{xy}^2(f) = \frac{|S_{xy}(f)|^2}{S_{xx}(f)S_{yy}(f)} \tag{4.1}$$

The cross-spectral density and power spectral density are the Fourier transforms of cross-correlation and auto-correlation respectively. For each pair of sensors, we compute the coherence using Welch's method [25], which is an improved estimator of the PSD. The method consists of dividing the time series into segments, computing a periodogram for each segment and then averaging the PSD estimates. The averaging of periodogram estimates tends to decrease the variance of the estimate in comparison to a single periodogram estimate of the whole data. A non-rectangular window such as a Hamming window is used to reduce the weight of end- samples in the segments.

For our experiments, we choose an epoch size(segment length) of 1 second and a Hamming window. The resultant signal is then analysed for five major frequency bands where most of the clinically relevant activities take place : alpha (8 - 13 Hz), beta (15 - 29 Hz), theta (4 - 8 Hz), delta (1 - 4 Hz), gamma (28-42 Hz)[23]. For each of the frequency bands, coherence is estimated as the average of coherence values in that interval. Let γ_k be the coherence estimate for the k_th frequency band. Then,

$$\gamma_k^2 = \frac{1}{BandLength} \sum_{f \in k} \gamma^2(f) \tag{4.2}$$

The coherence maps of the sensor space are given in figures 4.2 - 4.6. The white regions in the coherence map denote the sensor pairs with a coherence value greater than 0.9. The x and y axis corresponds to the sensor space. Hence, the intensity at a pixel (x, y) gives the coherence value between sensors x and y for that particular band. From the figures, it can be seen that the white region is concentrated along the

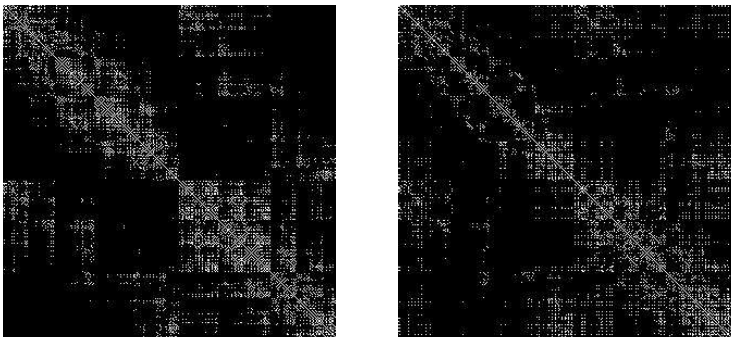

(a) epileptic (b) resting

Figure 4.2: Alpha Band

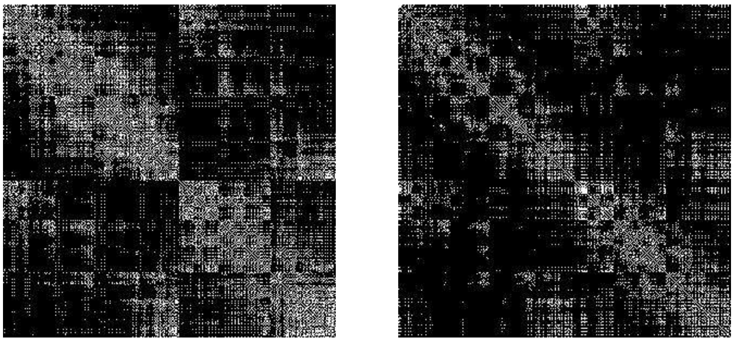

(a) epileptic (b) resting

Figure 4.3: Beta Band

diagonal. This is expected since diagonal entries represent adjacent sensors, and they are highly correlated due to MEG smearing. The point of interest, however, is the white blocks away from the diagonal. These regions show that there is coherence between regions not adjacent to each other. It can also be seen that the white regions increase for epileptic case, which shows an enhanced connectivity among the regions of the brain during epilepsy. The average coherence values for the five bands of interest are give in Table 4.1. As seen from the table, the average coherence values are higher for each of the bands in the epileptic state in comparison to resting state. Notably, beta band registers an increase of 35% in the epileptic case. Hence, it can be argued that, epilepsy indeed is characterised by an increase in coherence among various regions of the brain, which translates to enhanced connectivity which could be a possible cause for epilepsy.

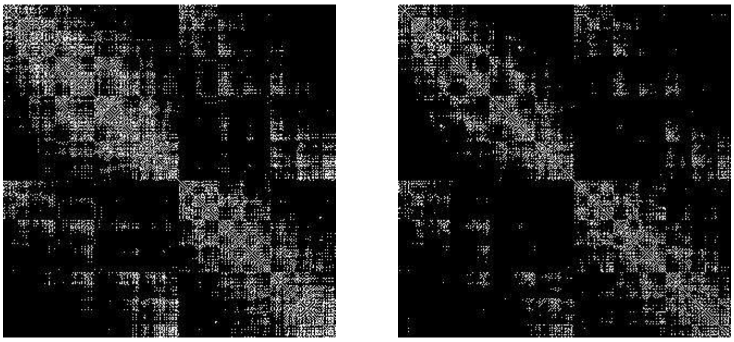

(a) epileptic (b) resting

Figure 4.4: Gamma Band

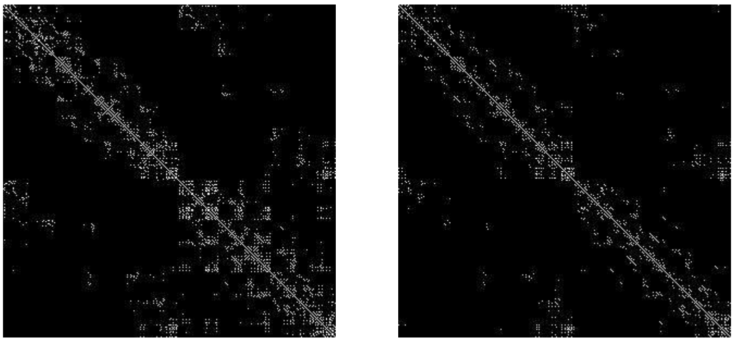

(a) epileptic (b) resting

Figure 4.5: Delta Band

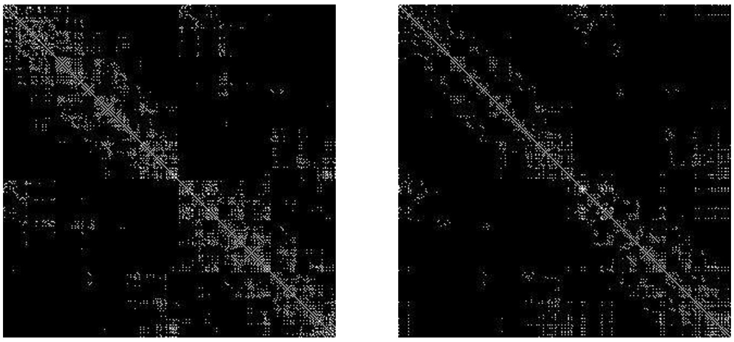

(a) epileptic (b) resting

Figure 4.6: Theta Band

Frequency Band	**Non-Epileptic**	**Epileptic**
Alpha	0.212	0.242
Beta	0.323	0.431
Delta	0.179	0.208
Gamma	0.334	0.378
Theta	0.189	0.208

Table 4.1: Average Coherence Values

4.2 Detection of Epileptic Regions

4.2.1 Graphical Analysis

In a healthy brain, the electrical activity is non-synchronous. This activity is controlled by the type, number and distribution of ion channels. However, changes in ion channels or malfunctioning of inhibitory neurons may cause the resistance of excitatory neurons to decrease. This is characterized by epileptic discharge where neurons fire with excessive synchrony.

Coherence analysis of the epileptic signals can be useful in detecting the epilogenetic regions in the brain. An epileptic episode is characterised by strong synchronisation of neuronal firing, which manifests in the coherence data. So a huge increase in coherence value between two sensors signifies that these sensors correspond to a source which is epilogentic. For our experiments, we analysed the MEG data before and during an epileptic discharge and marked the sensor pairs which showed an increase in coherence. We analysed the beta band alone, since this frequency band produced the most change in average epilepsy.

To group the sensor pairs corresponding to epileptic regions, we constructed a graph from the sensor space. The nodes of the graph denote the sensors, and edges denote the sensor pairs which marked an increase in coherence between the events. A graph which shows all sensor pairs which marks an increase in coherence would be a highly connected and dense graph, and would not help in segregating the sensor space. Hence we constructed graphs in such a way that an edge is formed between two nodes, only if the coherence value between the two nodes (sensors) marks an increase of $x\%$. The graph for $x = 400\%$ and $x = 1000\%$ is given in figure 4.7.

The epilogenetic sensors can be identified by analysing the connected components of the graph. If {sensor A, sensor B} and {sensor B, sensor C} are synchronised, we can conclude that {sensor A, sensor B, sensor C} represent similar excitatory regions. Hence, the epilogenetic sensors can be identified by analysing the connected the com-

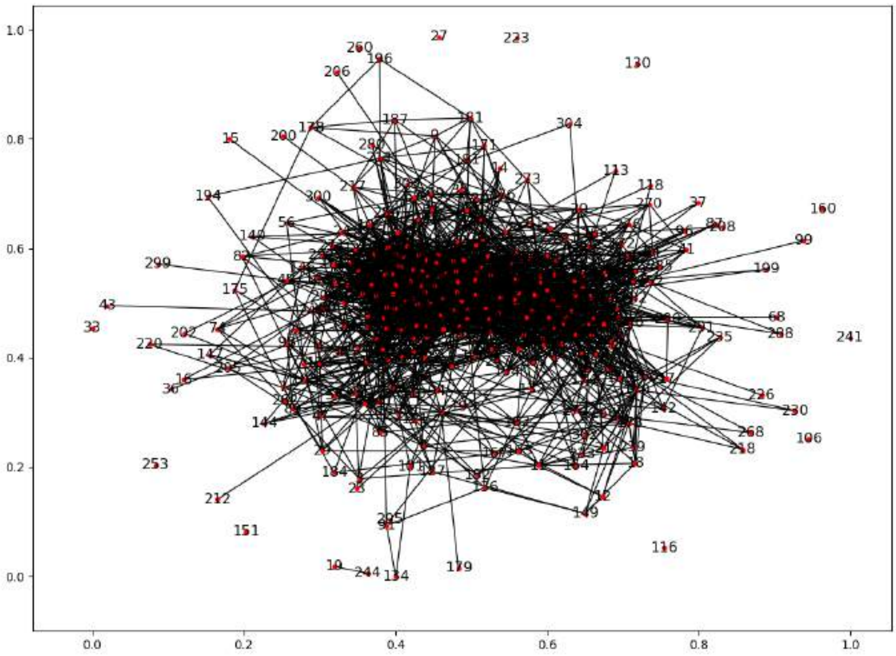

(a) 400 %

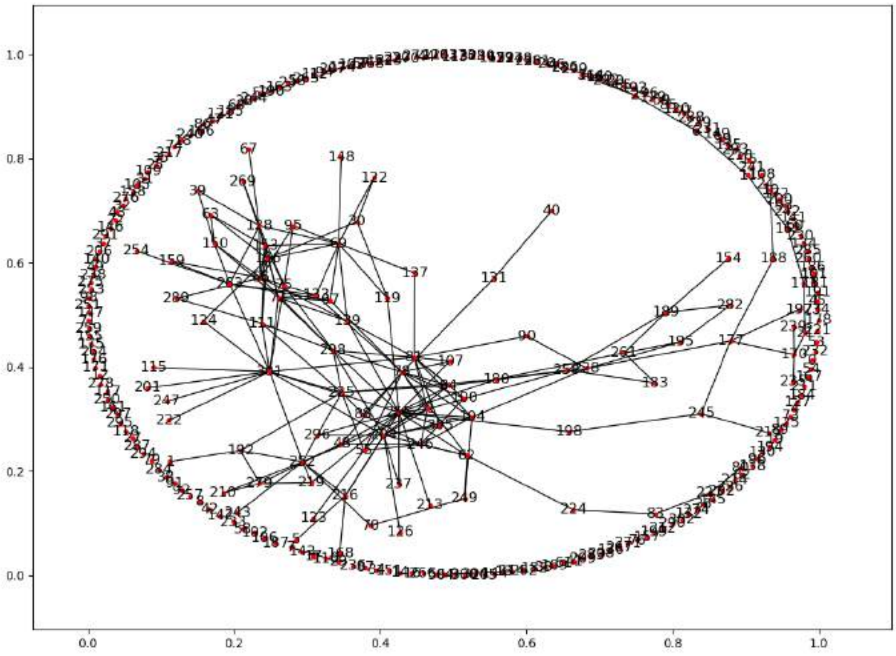

(b) 1000 %

Figure 4.7: Sensor coherence graphs. (a) Sensor pairs which marks an increase on 4 times in coherence (b) Sensor pairs which marks an increase of 10 time in coherence. The graph is highly connected in (a) and hence do not yield useful results

ponents of the graph. It was found that, 95 % of the sensors belonged to the same connected component for the 400 % case, while only 30 % of the sensors belonged to the same connected component for the 1000 % case. By defining a proper threshold, the epilogenetic sensors can be estimated. Data from several patients would be a useful resource to define a threshold.

4.3 Conclusions

In this chapter, we analysed the relationship between epilepsy and coherence between MEG sensors. We established that an epileptic discharge is characterised by increase in average coherence and subsequently an increase in connectivity among various regions of the brain. It is possible to identify the epilogenetic regions in the brain by analysing the increase in coherence values pre and post epilepsy. A graphical method for this analysis in the sensor space is also done.

As an extension, it will be interesting to map epilogenetic regions back to the brain. This would help a medical professional to analyse data efficiently. A source localisation needs to be performed to this end.This is an ill posed inverse problem of finding the region in the brain an MEG signal originates from. As a first step to this MRI-MEG coregistration, which maps a sensor into an MRI image. Once this is done our can be done to map the epilogenetic regions in the MRI.

It will also be interesting to analyse whether epilepsy is caused by increase in connectivity between regions. For this, the resting state MEG data of an epileptic patient needs to compared with that of a healthy subject

CHAPTER 5

Conclusions

In this thesis, the applications of image processing in various domains were examined. In particular, we addressed the problem of barrel distortion in wide eye fish eye lenses and the problem of rolling shutter distortion and motion blur in image super resolution. We also demonstrated the power of signal coherence in detecting epilogenetic regions in the brain.

In Chapter 2 we devised an algorithm to project images captured in the fish eye plane to the conventional rectilinear image plane. We also demonstrated generation of panorama from a pair of fish eye images. In Chapter 3, we formulated and solved the problem of super resolution in the presence of motion blur and rolling shutter effects. We used a parametric method to estimate the image trajectory during exposure. We also demonstrated the power of a good initial estimate on the final output, and devised a method for a good initial image estimate. In Chapter 4, we examined enhanced connectivity among regions of the brain during epileptic discharge using coherence between sensor pairs.

REFERENCES

[1] **R. Benosman and S. Kang**. *Panoramic Vision*. Springer Verlag. 2000; ISBN0-387-95111-3

[2] **Jonathan Courbon, Youcef Mezouar, Laurent Eck, Philippe Martinet**. *A Generic Fisheye camera model for robotic applications*. Proceedings of the 2007 IEEE/RSJ International Conference on Intelligent Robots and Systems.

[3] **Yu-Chuan Su, Dinesh Jayaraman, and Kristen Grauman** *Pano2Vid: Automatic cinematography for watching* 360^o *videos* . Proceedings of the Asian Conference on Computer Vision (ACCV), 2016

[4] **Xiaohui Wang, Kehe Wu and Shengzhuang Wang** *Research on Panoramic Image Registration Approach based on Spherical Model* . International Journal of Signal Processing, Image Processing and Pattern Recognition. 2013; 6(6): 297-308

[5] **Ellen Schwalbe** *Geometric Modelling and Calibration of Fisheye Lens Camera Systems*. Proceedings 2nd Panoramic Photogrammetry Workshop, Int. Archives of Photogrammetry and Remote Sensing

[6] **Juho Kannala and Sami S. Brandt** *A Generic Camera Model and Calibration Method for Conventional, Wide-Angle, and Fish-Eye Lenses*. IEEE Transactions on Pattern Analysis and Machine Intelligence. 2006;28(8): 1335-1340

[7] **David Claus and Andrew W. Fitzgibbon** *A Rational Function Lens Distortion Model for General Cameras*. Computer Vision and Pattern Recognition, 2005

[8] **S. C. Park, M. K. Park, and M. G. Kang** *Super-resolutionimage reconstruction: a technical overview*. Signal Processing Magazine, IEEE. 2003; 20(3):21-36.

[9] **R. Y. Tsai and T. S. Huang**. *Multipleframe image restoration and registration*. Advances in Computer Vision and Image Processing. 1984: 317-339.

[10] **J. Yang, J. Wright, T. Huang, and Y. Ma**. *Image super resolution via sparse representation* . Image Processing, IEEE Transactions on. 2010, 19(11): 2861-2873.

[11] **Chao Dong ; Chen Change Loy ; Kaiming He ; Xiaoou Tang**. *Image Super-Resolution Using Deep Convolutional Networks* . IEEE Transactions on Pattern Analysis and Machine Intelligence. 2016; 38(2): 295-307

[12] **Filip Sroubek, Gabriel CristÃşbal** *A Unified Approach to Superresolution and Multichannel Blind Deconvolution* . IEEE Transaction on Image Processing. 2007;16(9): :2322âĂŞ2332

[13] **C. Paramanand and A. N. Rajagopalan**. *Non-uniform Motion Deblurring for Bilayer Scenes*. IEEE Conference on Computer Vision and Pattern Recognition. 2013

[14] **Abhijith Punnappurath, Vijay Rengarajan, and Rajagopalan A.N**. *Rolling Shutter Super-Resolution*. International Conference on Computer Vision, 2015

[15] **Vijay Rengarajan, Abhijith Punnappurath, A.N. Rajagopalan, Gunasekaran Seetharaman** *Rolling Shutter Super-Resolution for Burst Mode*. IEEE International Conference on Image Processing. 2016

[16] **Rolf Kohler, Michael Hirsch, Betty Mohler, Bernhard Sch ÌĹolkopf, and Stefan Harmeling** *Recording and playback of camera shake: benchmarking blind deconvolution with a real-world database*. European Conference on Computer Vision. 2012: 27-40

[17] **Shuochen Su1, Wolfgang Heidrich**. *Rolling Shutter Motion Deblurring*.

[18] **Bressler SL and Kelso JA**. *Cortical coordination dynamics and cognition.*. Trends Cogn Sci. 2001; 5(1):26-36.

[19] **Susan M Bowyer**. *Coherence a measure of the brain networks: past and present*. Neuropsychiatric Electrophysiology. 2016: 2:1.

[20] **S. Ge, T. Wu, HY. Tang, X. Xiao, K. Iramina, and W. Wu**. *Coherence Analysis for Epilepsy Patients: An MEG Study* . World Academy of Science, Engineering Technology. 2011, Issue 56: 517.

[21] **T. Harmony, E. Marosi, T. FernÃąndez,J. Bernal, J. Silva, M. RodrÃ■guez, A. Reyes, A. FernÃąndez-Bouzas, M. Alonso, R. MendizÃąbal R,et al**. *EEG coherences in patients with brain lesions* . Int J Neurosci. 1994; 74: 203-226

[22] **F. Bartolomei, I. Bosma, M. Klein, J.C. Baayen, J.C. Reijneveld, T.J. Postma, J.J. Heimans, et al**. *How do brain tumors alter functional connectivity? A magnetoencephalography study* . Ann Neurol. 2006;59: 128-138

[23] **Jayabal Velmurugan, Sanjib Sinha, Parthasarathy Satishchandra**. *Magnetoencephalography recording and analysis*. Annals of Indian Academy of Neurology. 2014;17: 113

[24] **Samu Taulu and Riitta Hari**. *Removal of Magnetoencephalographic Artifacts With Temporal Signal-Space Separation: Demonstration With Single-Trial Auditory-Evoked Responses*. Human Brain Mapping. 2009;30: 1524-1534

[25] **KristÃ■na MezeiovÃą and Milan PaluÅą**. *Comparison of coherence and phase synchronization of the human sleep electroencephalogram*. Clinical Neurophysiology. 2012;123(9): 1821-1830

[26] **Adler G, Brassen S, Jajcevic A** *EEG coherence in Alzheimer's dementia*. J Neural Transm. 2003;110: 1051

[27] **ÃŰzerdem A, GÃijntekin B, AtagÃijn M, Turp B, BaÅ§ar E**. *Reduced long distance gamma (28-48 Hz) coherence in euthymic patients with bipolar disorder*. J Affect Disord. 2011;132: 325-332

[28] **Yeragani VK, Cashmere D, Miewald J, Tancer M, Keshavan MS**. *Decreased coherence in higher frequency ranges (beta and gamma) between central and frontal EEG in patients with schizophrenia: a preliminary report*. Psychiatry Res. 2006;141: 53-60

[29] **Brazier MA** *Spread of seizure discharges in epilepsy: anatomical and electrophysiological considerations.*. Exp Neurol. 1972;36: 263-172

[30] **Song J, Tucker DM, Gilbert T, Hou J, Mattson C, Luu P, et al**. *Methods for examining electrophysiological coherence in epileptic networks*. Front Neurol. 2013;4: 55

LIST OF PAPERS BASED ON THESIS

1. **Abhijith Punnapurath, Vijay Rengarajan, Green Rosh K S, A N Rajagopalan**. *Super Resolution with Motion Artefacts*. IEEE Transactions in Image Processing. (To be submitted)